Dendritic delay lines shape the computation of sound location in neurons of the gerbil medial superior olive

Authors/affiliations

Jared Casarez[1*], Rebecca I. Voglewede[1*], Bradley D. Winters[2], Ken Ledford[1] and Nace L. Golding[1]

* Equal contributions

[1] The University of Texas at Austin, Department of Neuroscience and Center for Learning and Memory, 1 University Station C7000, Austin TX 78712-0248, USA.

[2] Current address: Department of Biological Sciences and University Hospitals – NEOMED Hearing Research Center, Northeast Ohio Medical University, Rootstown, OH, 44272, United States and Brain Health Research Institute, Kent State University, Kent, OH, 44242, United States

Corresponding author and lead contact

Nace L. Golding: The University of Texas at Austin, Department of Neuroscience and Center for Learning and Memory, 1 University Station C7000, Austin TX 78712-0248, golding@austin.utexas.edu.

ABSTRACT

In mammals, neurons of the medial superior olive encode information about sounds arising from discrete spatial locations along the horizon. This tuning requires that an internal delay in the brain must offset acoustic disparities to ensure coincident arrival of excitatory inputs driven from the two ears. The source of this optimal internal delay, originally assumed to arise from axonal delay lines, is currently controversial in mammals. Here we use 2-photon guided paired dendritic and somatic recordings together with compartmental modeling of 40 complete MSO neuron morphologies to demonstrate that the dendrites themselves serve as a significant source of internal delay. We show that most MSO neurons exhibit morphological asymmetries that impose different EPSP delays across dendrites and shifts in optimal interaural time differences. Dendrite-based delays in the mammalian MSO are heterogeneous within each isofrequency laminae and provide a stable, structural mechanism to help tune individual neurons to sounds from different azimuthal locations.

KEYWORDS

dendrite; dendritic filtering; coincidence detection; auditory; sound localization.

INTRODUCTION

Spatial information in the auditory system is critical for humans and other mammals to assemble a 3-dimensional view of the world as well as to understand speech and communication signals, especially in environments with many sounds overlapping in time and in frequency. The auditory system is distinct from vision or touch in that there is no explicit peripheral representation of space, in this case in the cochlea, only a representation of frequency. Accordingly, the central auditory system must compute horizontal sound location indirectly by combining a series of monaural and binaural cues (Grothe and Pecka, 2014; Joris and Yin, 2007) . Spatial coding in the central auditory system is a prime example of a centrally synthesized or computational map.

Interaural time difference cues are used by birds and mammals to compute horizontal sound location at low frequencies (Carr et al., 2001) . In mammals this computation takes place in the medial superior olive (MSO), whose neurons are the first to receive converging excitatory and inhibitory inputs driven from the two ears. Intriguingly, in individual neurons, binaural inputs are integrated within a bipolar dendritic architecture, with ipsilateral and contralateral excitatory inputs segregated onto lateral and medial dendritic branches respectively (Lindsey, 1975; Stotler, 1953) . Ipsilateral and contralateral inhibition converges onto the soma and proximal dendrites (Kapfer et al., 2002; Lindsey, 1975; Magnusson et al., 2005; Stotler, 1953; Yin and Chan, 1990) . MSO neurons detect the optimal combination of these inputs, converting temporal coincidence into a rate code (Goldberg and Brown, 1969; Spitzer and Semple, 1995; Yin and Chan, 1990) .

The concept of internal delay is central to coincidence detection in the MSO, where acoustic delays to the two ears are countered in time by a mechanism of delay inside the brain. This internal temporal asymmetry was postulated in early models to arise from axonal delay lines formed by ladder-like combinations of bilateral excitatory inputs (the "Jeffress model") (Jeffress, 1948) . While the Jeffress model enjoys strong support in birds (Carr and Konishi, 1990, 1988; Moiseff and Konishi, 1981) , comparable studies in mammals have failed to reveal systematic axonal input delay lines nor any mapping of delay along the nucleus (Beckius et al., 1999; Smith et al., 1991; Yin and Chan, 1990) . More recently, there is evidence that fast inhibition mediates internal delay by shifting the peaks of EPSPs (Brand et al., 2002; Myoga et al., 2014; Pecka et al., 2008) . However, this mechanism is subject to vigorous debate (Franken et al., 2015; Heijden et al., 2013; Roberts et al., 2013) , and it is not clear that this mechanism alone can explain the range of receptive field locations in the MSO or their insensitivity to sound level. Other mechanisms have been proposed to mediate internal binaural asymmetry, including asymmetrical axon position, medio-lateral differences in the rising slopes of EPSPs (Jercog et al., 2010), and differences in tuning of binaural inputs ("stereausis") (Plauška et al., 2017; Shamma et al., 1989).

All models of coincidence detection must address the issue of the temporal distortions imposed by the dendrites themselves. However, to date models of MSO neurons have been represented either as point neurons or as simplified, symmetrical "ball-and-stick" models (Agmon-Snir et al., 1998; Callan et al., 2021; Dasika et al., 2007; Franken et al., 2014; Mathews et al., 2010; Myoga et al., 2014) . Previous measurements of dendritic propagation have revealed that EPSPs encounter delays in their propagation to the soma

86 up to ~150 μs, despite some degree of temporal compensation by activation of low
87 voltage-activated K channels in the soma and proximal dendrites (Mathews et al., 2010) .
88 However, these measurements have largely been restricted to the proximal half of the
89 dendritic arbor and have relied on averaging highly variable populations of neurons. Given
90 that the dendrites of MSO neurons alter their branching pattern and diameters during
91 early hearing and following disruptions of normal hearing (Feng and Rogowski, 1980;
92 Russell and Moore, 1999; Smith and Rubel, 1979), they might serve as a potential
93 mechanism for adjusting the timing requirements for sounds from the two ears to arrive
94 coincidently at the soma and axon.

95 Here we demonstrate that the dendritic arbors of MSO neurons are highly heterogeneous
96 and show a striking continuum of asymmetry across the medial and lateral branches that
97 receive segregated inputs driven respectively from the two ears. We show with dual 2-
98 photon fluorescence-guided patch recordings that inputs to smaller and/or more distal
99 dendrites show more substantial propagation delays than previously recognized, and
100 computational modeling of a large population of intact neuronal morphologies shows that
101 these dendritic asymmetries translate into stable internal delays that, as a population,
102 could account for the full range of naturally occurring horizontal locations. Finally, we
103 show that inhibition preserves the effects of dendritic asymmetry on interaural time
104 differences (ITDs) and helps bring the region of maximum slope of firing changes within
105 the ecologically relevant range. Thus dendrite-based delay lines likely work synergistically
106 with other integrative mechanisms purported to shape the perception of horizontal
107 position in mammals.

108

RESULTS

To understand how MSO neurons process interaural time differences in the dendrites, we made fluorescence-guided dendritic and somatic patch-clamp recordings visualized under 2-photon microscopy. Using this approach, we were able to target the distal third of the dendritic arbor, including secondary and tertiary branches, regions that have largely escaped investigation in these neurons. We then injected simulated EPSCs (τ_{rise} and τ_{decay}, 0.2 ms) into the dendritic pipette and recorded potentials simultaneously at both dendrites and soma. We observed strong variability in both the percent amplitude attenuation at the soma $\left(\left(\frac{V_{soma}}{V_{dend}}\right) \times 100\right)$ as well as the propagation delay of the EPSP,

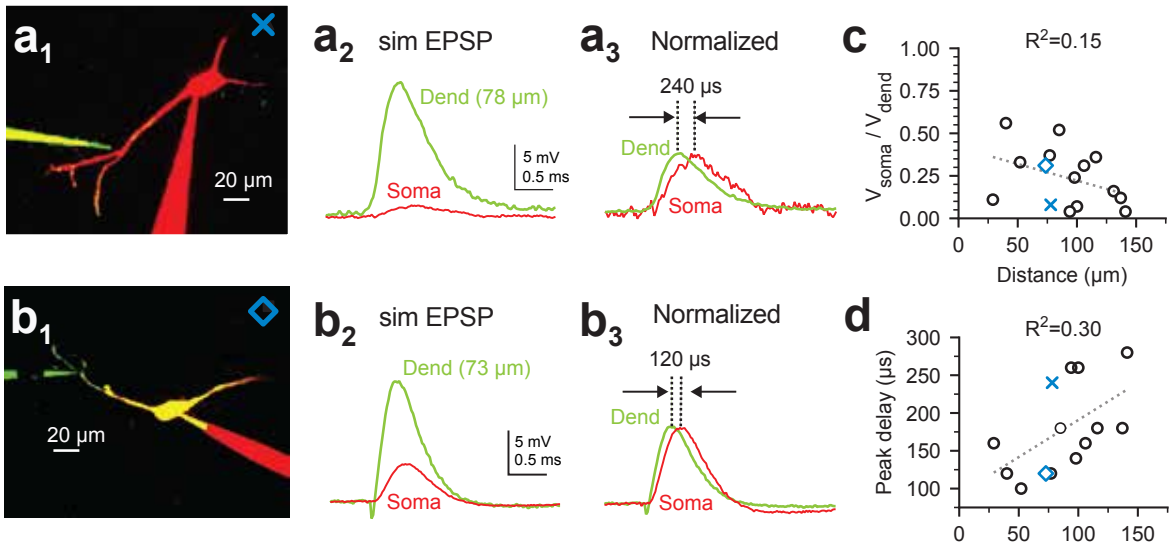

Fig. 1: Heterogeneity in attenuation and timing of simulated excitatory synaptic potentials following propagation from distal dendritic locations to the soma.
a,b, 2-photon fluorescence-guided dual dendritic and somatic patch recordings from two MSO neurons of comparable distances (78 and 73 µm, respectively). Example neuron in **a**$_1$ shows stronger attenuation of somatic propagation of a simulated EPSP (**a**$_2$ vs. **b**$_2$) and longer peak delay (**a**$_3$ vs. **b**$_3$). EPSC amplitudes: cell **a**, 600 pA; cell **b**, 400 pA. **c,d**, Group data for attenuation and peak delay for all paired MSO neuron recordings. There is a poor correlation of both measures as a function of distance.

measured as the difference in EPSP peak time at the soma relative to the dendrite (Fig. 1). Notably, the delays measured in these recordings ranged between 100 and 300 µs, exceeding the physiological range of ITDs measured in gerbils. In these recordings,

121 there was little correlation between local morphological features of recorded dendrites
122 and propagation delay of the EPSP, measured as the difference in the peak timing of
123 dendritic and somatic EPSPs (Fig. 2a-c). However, there was a stronger correlation
124 between the local dendritic membrane time constant and EPSP propagation delay (Fig.
125 2d). In addition, there was a weak trend of increasing dendritic membrane time constant

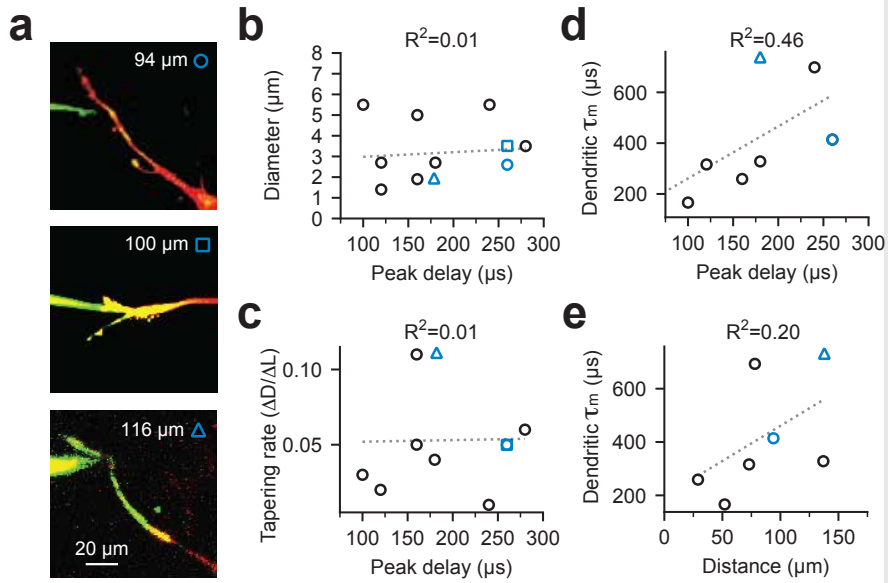

Fig. 2: EPSP propagation delays are not correlated with local morphology but rather more global physiological properties. **a**, Closeups of distal dendritic morphology during paired dendritic and somatic recordings. **b,c**, Delay of peak EPSPs during propagation from dendrite to soma shows no significant correlation with local diameter or tapering rate of local dendrite. (dendritic EPSCs: 400-1000 pA). **d**, Peak EPSP delay from dendrite to soma was weakly correlated with the membrane time constant recorded at the dendritic recording site. **e**, Dendritic membrane time constant increased with distance of the recording site from the soma.

126 with recording distance (Fig. 2e), possibly because of proximity to the dendritic
127 terminations. These results may reflect that an understanding of the integrative properties
128 of the dendrites requires an analysis of the larger morphological and electrotonic structure
129 of the neuron.

130 To understand how overall dendritic structure impacts binaural coincidence detection, we
131 analyzed a database of biocytin-filled MSO neurons that exhibited complete dendritic
132 structures (40 of 270 neurons from Bondy et al., 2021 (Bondy et al., 2021) ; Fig. 3). We
133 quantified dendritic length, surface area and branching, with special emphasis on
134 comparisons of medial and lateral dendritic arbors. Higher-order (2° and higher) dendritic

135 branches were prominent in these neurons, comprising 70% of the membrane surface
136 area (Fig. S1).

137 A striking feature of most neurons in this data set was an overall asymmetry between the
138 lateral and medial dendritic arbors, reflecting differences in length, branching, and/or
139 diameter of the dendrites (Fig. 3a-c). We quantified this asymmetry according to two

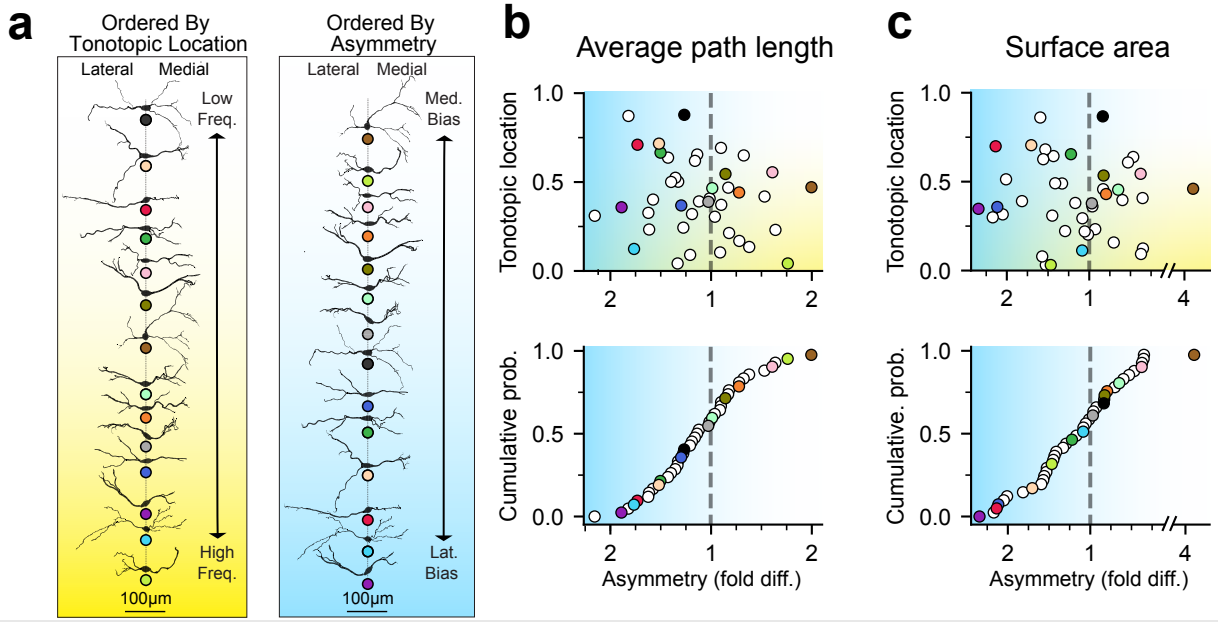

Fig. 3: MSO neuron morphology is inhomogeneous and asymmetric, regardless of tonotopy.
a, Reconstructed morphologies rank ordered by tonotopy (left) and degree of asymmetry (right; average path length). Orderings span from low frequency (top) to high frequency (bottom) and medial (top) and lateral (bottom) asymmetry, respectively. Colored gradients added to visualize ordering. Uniquely colored dots placed beneath each morphology for differentiation. **b**, Fold difference between average path length of medial and lateral dendrites for all reconstructed morphologies (n=40) with vertical axes ordered by tonotopic location (top) or degree of asymmetry (bottom). Gradients added as in **a**. Colored points correspond to **a**. **c**, Same as **b**, except comparing total surface area of medial and lateral branches. Average medio-lateral path length and surface area fold differences (± SEM) were 1.080 ± 0.057 and 1.112 ± 0.133 (biased laterally) and tonotopic R^2 values were -0.42 and -0.23.

140 parameters, the average path length (average length from each dendritic end to the
141 soma) and membrane surface area, with the latter parameter reflecting the collective
142 influence of dendritic length, diameter and branching pattern. We then defined the degree
143 of bilateral asymmetry as fold differences between the larger vs. smaller dendritic
144 measure for each parameter. We observed no obvious correlation between dendritic
145 asymmetry and tonotopic location (Fig. 3a, *left* and 3b, *top*). However, we found that

146 dendritic asymmetry formed a finely graded continuum, with a slight bias toward lateral
147 dendrites (Fig. 3b, *bottom*). Interestingly, there were no significant differences in
148 population averages of the medio-lateral path length and surface area (1.080 ± 0.057 and
149 1.112 ± 0.133 fold differences; p=0.562), though there was a slight lateral bias. These
150 results indicate that the averaging of dendritic morphological parameters across neurons
151 obscures what is likely a key structural and computational feature.

152 To understand how morphological asymmetry impacts synaptic integration, we
153 constructed compartmental models using the same 40 reconstructions analyzed in Fig. 3.
154 We introduced an excitatory synaptic conductance (alpha function: τ = 290 μs) into each
155 dendritic compartment and then measured the voltage attenuation and propagation delay

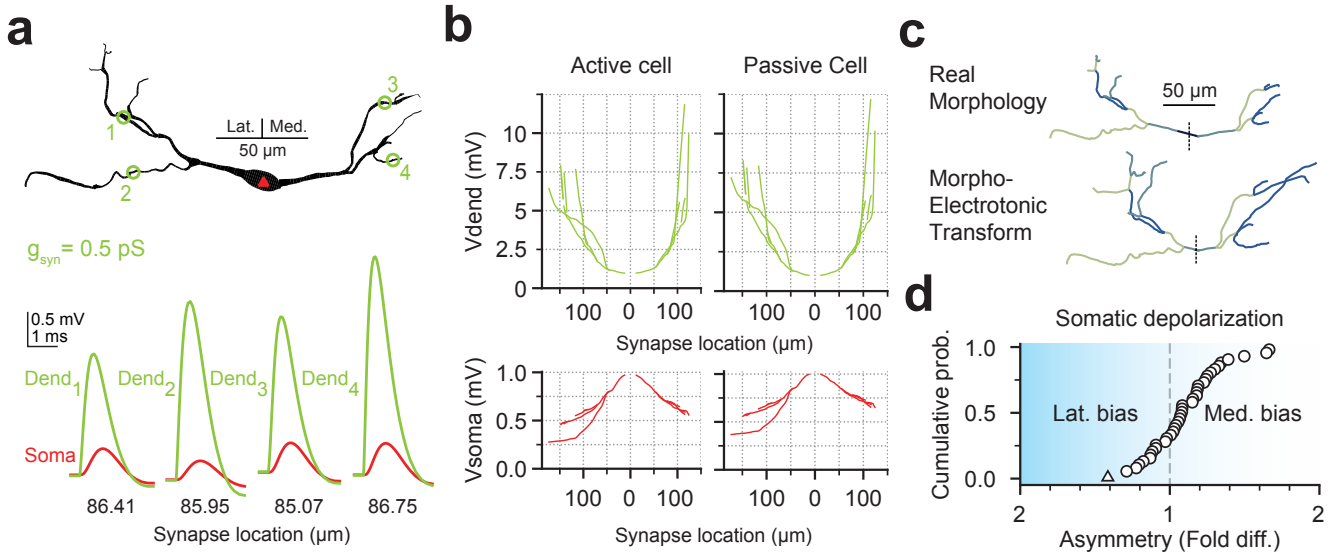

Fig. 4: MSO morphology nonlinearly filters and attenuates propagating EPSPs through its passive cable properties.
a, Visualization EPSP filtering at different dendritic sites. Cell morphology (top) with similarly distant example synaptic sites indicated with green circles and corresponding numbers. Red triangle indicates the somatic compartment. Synaptic conductance indicated as g_{syn}. Four sets of paired dendritic (green) and somatic (red) traces (bottom) for each example synaptic site. Numbering of traces corresponds to labels on morphology above. Dendritic distance from soma for each site indicated below traces. **b**: Same procedure as in **a**, with an adjusted unitary synaptic conductance (see Methods), with measurements from each computational compartment. Model morphology and orientation same as in **a**. Comparison between active channel (left) and passive channel model (right). Recorded EPSP amplitude at synaptic (top, green) and somatic (bottom, red) compartment as a function of distance from soma. **c**, Actual (top) and electrotonically transformed (bottom) morphologies. Transformation visualizes degree of EPSP attenuation from each compartment (see Methods). **d**, Group data (n=40) of average somatic depolarization asymmetry between mediolateral sides. Gradient as in Fig 3. Dotted line indicates equal medial and lateral average somatic depolarizations. Cell from **a-c** indicated with a triangle.

156 from the dendritic input location to the soma (Figs. 4-5). At comparable distances from
157 the soma, EPSP amplitude at the site of synaptic input and following propagation to the
158 soma varied considerably, like the physiological data from paired recordings in Figure 1
159 (Fig. 4a). Plots of local dendritic and propagated somatic EPSP amplitudes across all
160 synapse locations further revealed striking asymmetries in propagation efficacy of EPSPs
161 to the soma (Fig. 4b, “Active cell”). In MSO neurons, the timing and attenuation of EPSPs
162 along dendrites are influenced both by passive cable filtering as well as interactions with
163 low voltage-activated K channels, which are active in the subthreshold voltage range in
164 these neurons (Mathews et al., 2010) . To determine the degree to which asymmetries in
165 low voltage-activated K channels impact EPSP attenuation at the soma we converted all
166 voltage-activated conductances to leak channels (Fig. 4b, “Passive cell”; see Methods).
167 While EPSPs propagated slightly more effectively to the soma from all dendritic locations
168 in the passive model, it did not fundamentally disrupt mediolateral asymmetry, indicating
169 that these differences arose primarily from the passive electrotonic architecture of the cell.
170 The branching structure had a significant effect on dendritic propagation asymmetry. This
171 could be better visualized in inward morphoelectrotonic transforms of cells, which exhibits
172 dendritic compartments according to their electrotonic, versus physical lengths. In the
173 example neuron in Fig. 4c, large primary dendrites are deemphasized, while thinner
174 secondary and tertiary branches appear as electrotonically elongated. Differences
175 between the medial and lateral dendritic arbors in this neuron and many others gave rise
176 to asymmetries in the magnitude of the average EPSP arriving at the soma.

177 Further, we observed that our population of cells formed a continuum in the degree of
178 somatic depolarization asymmetry, in line with the asymmetry in dendritic structure (Fig.

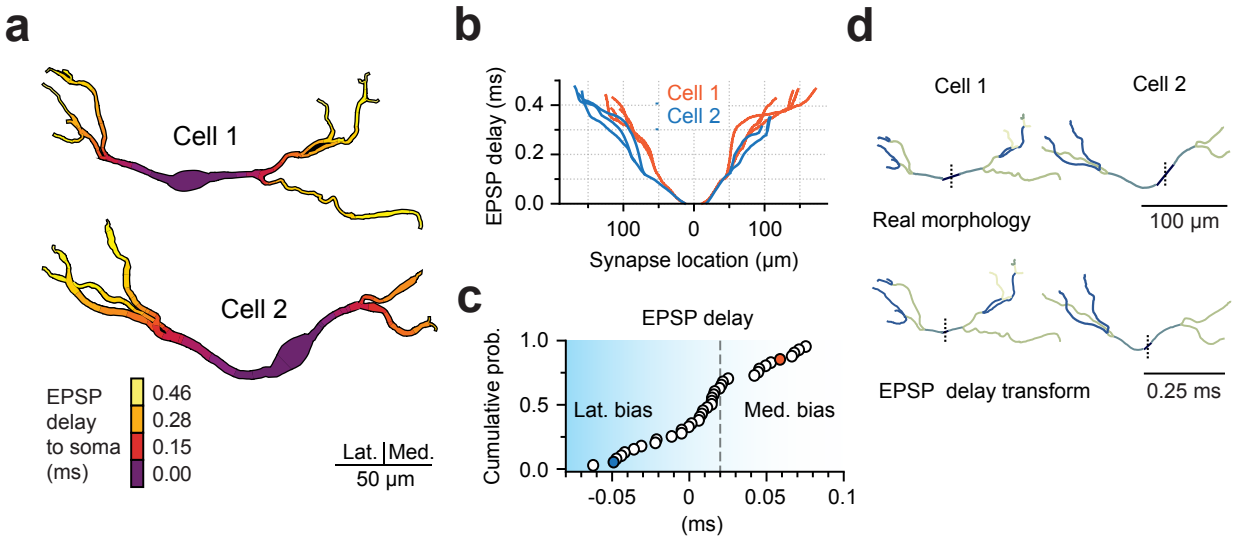

Fig. 5: EPSP timing significantly varies within and between cells, with morphological asymmetry informing overall cell timing. **a,** EPSP delay visualization in two exemplar MSO neurons. Coloring of each cell corresponds to the propagation delay of EPSPs to the soma from its respective compartment. Legend of propagation delay coloring in top right. Cells are oriented mediolaterally according to the scale bar. Outline added to increase gradient readability. **b,** Same data as in **a**, except as a function of distance from the soma. Orientation of cells same as in **a. c**, Group data (n=40) of the difference in average EPSP propagation delay between medial and lateral dendrites. Cells 1 & 2 are indicated with same color as in **b**. Dotted line at 0 ms indicates an equal average EPSP delay between sides. Blue gradient along horizontal axis (as in Fig. 3) to indicate spectrum of asymmetry. **d**, Morphological transforms according to EPSP delays. Morphological centroids of actual cell morphologies (top) and transformed morphologies (bottom). Length corresponds to each sections EPSP delay contribution. Coloring of cell sections is consistent between actual and transformed morphologies for easier differentiation and comparison. Dotted line added to mark the midline.

4d). Dendritic asymmetry also translated into differences in average EPSP timing across the medial and lateral dendrites. Figure 5a shows for two example neurons the spatial profile of delays of EPSPs propagating from each dendritic compartment to the soma. The asymmetry in dendritic timing can be more quantitatively visualized in plots of peak EPSP delay ($t_{dend} - t_{soma}$) as a function of dendritic distance from the soma (Fig. 5b). Dendritic branch points often introduced substantial jumps in propagation delays, and this is reflected in these plots as increases in slope. To quantify the influence of dendritic asymmetry on the optimal summation of bilateral EPSPs at the soma, we measured the electrotonic delay at the soma for every 2 µm compartment of lateral and medial dendritic subtrees. In our population of 40 neuron models, there were differences in the average relative time of arrival of EPSPs to the soma from compartments in the medial and lateral

190 dendrites. Further, these differences formed a smoothly graded continuum of delays
191 (Fig. 5c).

192 MSO neurons exhibit a range of intrinsic electrical properties, and so we examined a
193 subset of neuron morphologies to understand the functional implications of this
194 physiological diversity. Using a neuron with an asymmetric dendritic arbor, we
195 systematically slowed the membrane time constant by reducing the density of both low
196 voltage-activated K channels and HCN channels (Fig. S2). In both cases, the timing of
197 EPSPs reaching the soma was linearly related to the value of the membrane time
198 constant. Thus, the effects of dendritic asymmetry on EPSP timing and amplitude at the
199 soma are expected to be substantially higher in MSO neurons with slower intrinsic
200 membrane properties. To understand how the differential timing of EPSPs propagating
201 from medial and lateral dendrites is translated into ITDs, we simulated binaural excitatory
202 input using a spiking model of MSO neurons (see Methods). This model featured one
203 axonal input per terminal branch segment as well as a centripetal (dendrite-to-soma)
204 pattern of dendritic innervation, running from the terminal compartments to the soma, in
205 accordance with results from anatomical studies (Fig. 6a) (Beckius et al., 1999; Callan et
206 al., 2021; Smith et al., 1991). The conduction velocity of these inputs was set to 1 ms^{-1},
207 approximating values of unmyelinated terminal axonal arborizations of similar
208 caliber (Carr and Konishi, 1990; Hoffmeister et al., 1991) . The timing of ipsilateral and
209 contralateral inputs was varied systematically, triggering spiking only when the two inputs
210 were in close coincidence (Fig. 6b). The location of these excitatory ITD functions were
211 dependent on medio-lateral asymmetry. Functions shifted toward the side of the
212 electrically longer dendrite, reflecting the need for earlier activation of that side to

compensate for a longer dendritic propagation delay (Fig. 6c). Our population of 40

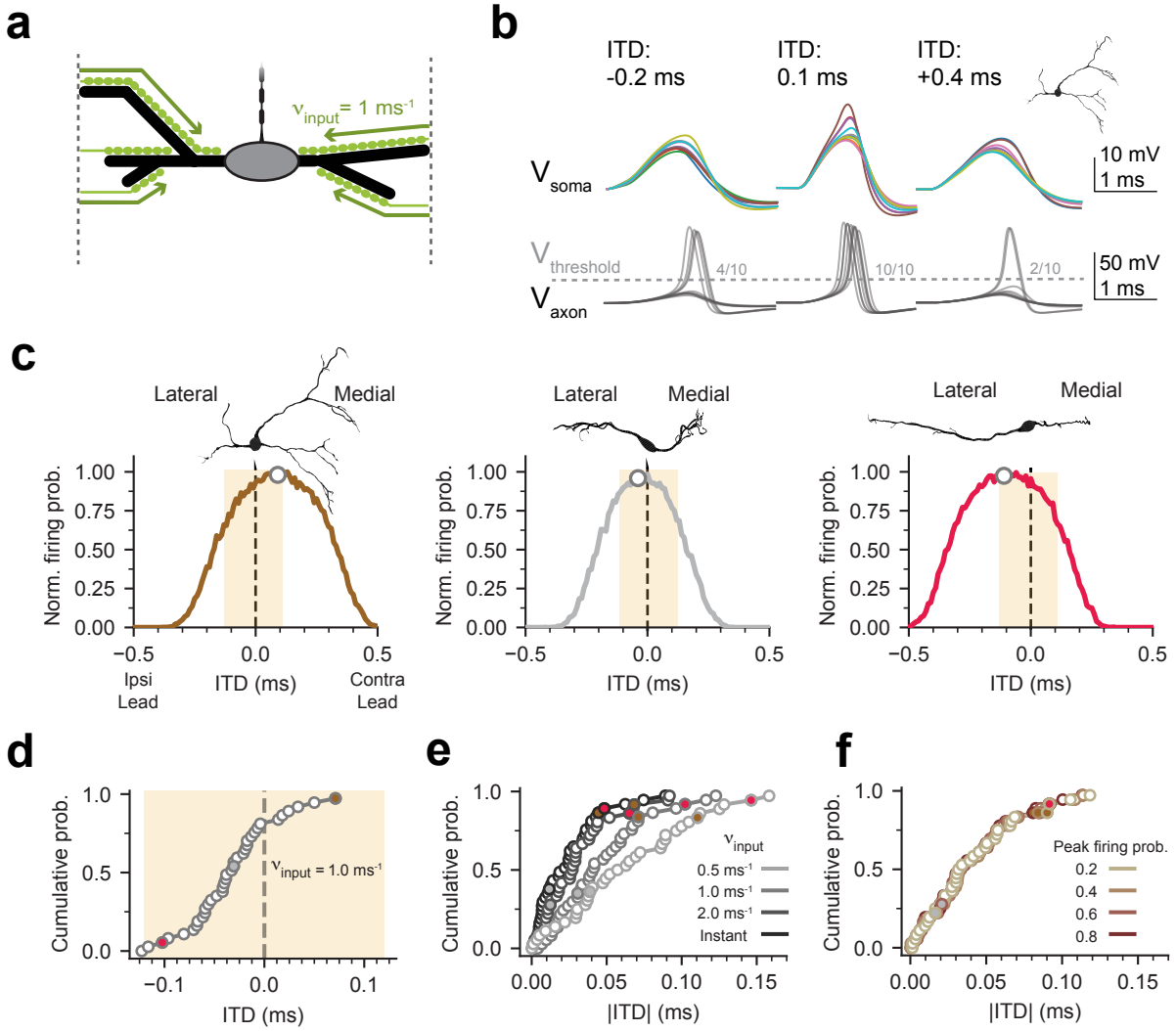

Fig. 6: Simulated ITDs demonstrate conservation of morphological impact on coincident detection. **a**, Schematic visualization of ITD innervation. Somatic compartment and dendrites are shown in gray and black, respectively. Green bulbs represent excitatory synapses, with corresponding arrows to illustrate axonal input velocity (v_{input}). Dotted lines illustrate point at which there is considered to be no axonal input delay (see Methods). Axon attached to soma, with initial segment, nodes, and internodes. **b**, Example somatic (top) and axonal (bottom) traces from ITD simulations. ITDs of -0.2 ms (left), 0.1 ms (middle, optimal coincidence), 0.3 ms (right) shown. Traces colored only for differentiation. Dotted line ($V_{threshold}$) indicates depolarization threshold for action potential consideration. Morphology of model cell indicated in upper right. **c**, Three example ITD firing curves from varied morphologies, medially biased (left), symmetrical (middle), and laterally biased (right). Corresponding morphologies imaged above. Light orange span represents range of ecologically possible ITDs for model species. Dashed line placed at ITD of 0 ms. Dot indicates centroid ITD value. **d,** Sorted group data (n=39) of centroid ITDs, with v_{input} = 1 ms^{-1}. Cells from **c** indicated with filled colored points. **e,f**, Sorted group data (n=39) of absolute centroid ITDs, varying axonal input velocity (**e**) and peak firing probability (**f**). Cells from **c** indicated with correspondingly filled colored points.

neurons showed peak firing at delays that traversed a continuum of values (-0.11 to 0.08 ms, median -0.02; Fig. 6d; Fig. S3). The precise range of values depended in part on the

assumptions on the velocity of excitatory axons. The largest range of ITDs was achieved when there was closer matching between the velocity of axonal input velocity and postsynaptic EPSPs propagating from the dendrites to the soma, which maximized temporal coincidence at the soma of spatially disparate inputs in the dendrites (Fig. 6e). Finally, ITDs shifted less than 3% in the face of input amplitude changes that resulted in firing probabilities between 0.2 and 0.8, indicating that dendritic asymmetry is highly stable across changing stimulus conditions.

Inhibition is a critical component of ITD encoding, although its precise role is subject to vigorous debate. To understand how dendritic asymmetry impacts the effects of inhibition, we added bilateral inhibitory conductances to the somatic compartment of the bilateral excitatory model in Fig. 6, consistent with the known somatically biased innervation of MSO neurons from the lateral and medial nuclei of the trapezoid body (LNTB and MNTB; (Kapfer et al., 2002; Werthat et al., 2008)). We set the timing of inhibitory conductances to be 500 μs in advance of excitatory inputs from the same side, in accordance with a previously published estimate (Roberts et al., 2013) . We then adjusted the amplitude of inhibitory conductances to produce summed IPSPs of between ~1-3 mV, which reduced firing probability by 20, 40, 60 and 100% (Fig. 7a). With increasing amplitude of IPSPs, resultant ITD functions decreased in halfwidth by 57%, but the location of functions with increasing levels of inhibition were not significantly different from the model with only excitatory inputs (0.070-0.078 ms; centroid, p=0.984; group data). However, the region of maximum slope consistently shifted towards zero, in accordance with a sinking iceberg receptive field scenario (Fig. 7d; -0.27 to 0.07 ms). We then tested how the relative timing of excitatory and inhibitory inputs altered ITD functions. Varying

239 the timing of IPSPs relative to EPSPs from –0.5 ms to 0.25 ms altered the location of ITD
240 functions by 0.04 ms, from 0.07 to 0.11 ms. Over the population of MSO neuron
241 morphologies, the presence of inhibition reduced firing probability without fundamentally
242 shifting the location of ITD functions. However, the region of the function where there is
243 maximal change in firing rate is necessarily impacted by the decrease in ITD width (Fig.
244 S4), suggesting that dendritic asymmetry and inhibition provide separate contributions to
245 MSO neurons' receptive field locations.

246

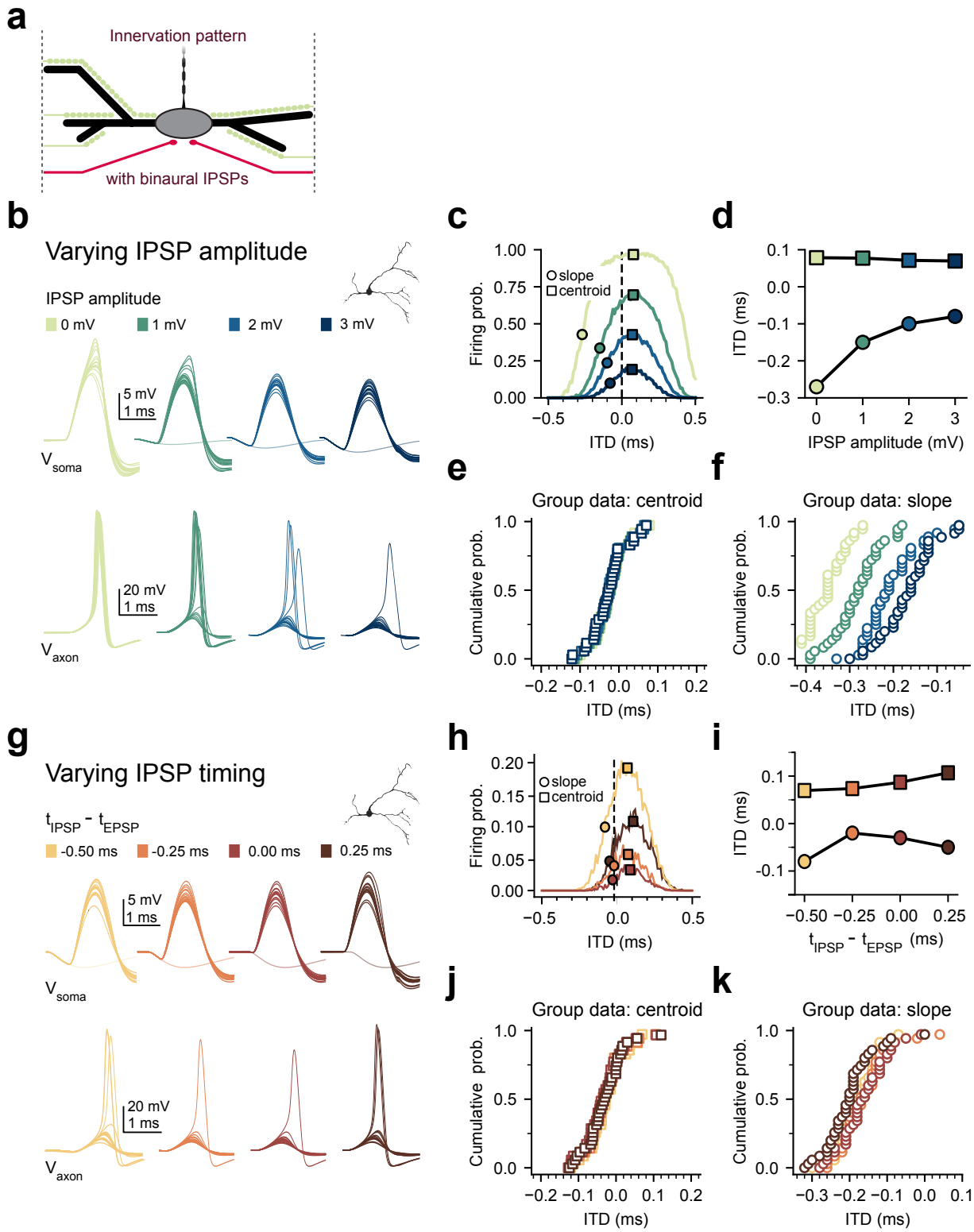

Fig. 7: Inhibition may serve to modulate a pre-established morphological baseline ITD response.
a, Schematic of innervation pattern with excitatory (green) and inhibitory (red) inputs. **b,** Somatic (top) and axonal (bottom) traces from ITD stimulation (ITD: 0.1 ms; IPSP timing: -0.5 ms) for each tested IPSP amplitude. Tested amplitude values and their unique colors above corresponding traces. Morphology of the exemplar neuron shown in the upper right. **c,** Exemplar cell's ITD response curves colored corresponding to IPSP amplitude in **b.** Centroid (square) and maximum slope (circle) are indicated for each curve. Dotted line at an ITD of zero. **d,** ITD centroid and maximum slope as a function of IPSP amplitude (colors corresponding to **b**). **e,f**, Group data (n=39) for ITD centroids (**e**) and steepest sections (**f**) for each IPSP amplitude. Data in **e** are largely overlapping. Shifting of population data in **f** corresponds to trend seen in the exemplar cell (**d**). **g-k**, Same as **b-f**, instead varying the timing of the inhibition (IPSP amplitude: 3 mV). Absolute firing probability, in **h**, is lower than **c**, resulting in lower signal to noise ratio. Centroids in **i** show more variation than **d**, though still minimal. Shift of exemplar cell's maximum slope ITD section (**i**) corresponds to degree of reduction in absolute firing probability (**h**).

247

DISCUSSION

The passive cable properties of neuronal dendrites are known to impart both attenuation and delay on EPSPs as they propagate to the soma, commensurate with the distance traversed and the anatomical features of the dendrite itself. However, the functional significance of dendritic geometry and its impact on action potential firing is often difficult to assess. Here we have newly identified a critical function for dendritic structure in the processing of sound localization cues in MSO neurons of the auditory brainstem. We have shown that the bipolar dendritic arbor of MSO neurons is typically asymmetrical, imposing a corresponding asymmetry in the relative timing required for excitatory inputs to drive optimal patterns of action potential output. Our compartmental models show that variation in dendritic morphology across cells exerts a continuum of temporal influences sufficient to shift spatial receptive fields across the full biological range of ITDs available to the gerbil. These shifts are insensitive to differences in intensity and likely work together with other sources of internal delay to enable MSO neurons to stably encode spatial locations along the horizontal plane.

Role of dendritic-based delays in the detection of input sequences

The idea that dendritic structure could dictate detection of temporal sequences of input was first explored in the pioneering computer models of Wilfred Rall. These studies showed that attenuation and propagation delays of EPSPs traveling from the dendrites to the soma could impart greater sensitivity to somatically vs distally directed activation sequences of excitatory inputs, where the longer propagation time of more distal EPSPs is compensated by their earlier activation (Rinzel and Rall, 1974) . Preferential firing to

270 centripetal (distal to proximal) temporal sequences of uncaged glutamate at spines has
271 been demonstrated in cortical neurons in slices, but it is not clear what natural conditions
272 would generate such sequences (Branco et al., 2010). By contrast, single excitatory
273 axonal inputs to MSO dendrites mediate a natural centripetal sequence of synaptic
274 activity (Beckius et al., 1999; Callan et al., 2021; Smith et al., 1993) , and both current
275 and previous modeling results highlight the importance of matching of input sequence
276 conduction velocity with that of MSO dendrites, which conduct EPSPs at an average of
277 ~0.3 ms^{-1}. In the present study, with the aid of 2-photon fluorescence-guided recordings
278 we have been able to sample smaller diameter secondary and tertiary dendrites at longer
279 distances from the soma. Our results reveal that the attenuation and delays of EPSPs
280 propagating from these processes to the soma are more severe than previously
281 estimated (Winters et al., 2017) . In our sample of modeled MSO neurons, these slower-
282 conducting non-primary dendrites make up 70% of the surface area of the dendritic arbor
283 in our sample of MSO neurons and thus play an outsized role in exerting temporal shifts
284 in ITD curves in neurons with asymmetrical dendritic trees. These results emphasize that
285 both branching and dendritic diameter are critical determinants of dendritic delay, as seen
286 reflected in the morphoelectrotonic transforms (Fig. 5). Earlier work reported systematic
287 bilateral asymmetries in excitatory input dynamics and apparent synaptic reversal
288 potentials in MSO neurons (Jercog, 2008; Jercog et al., 2010), which were interpreted as
289 reflecting differences in electrotonic length and synaptic location between medial and
290 lateral dendrites. These functional asymmetries are consistent with the dendritic
291 propagation delays measured here, suggesting that dendritic filtering may underlie
292 previously observed excitatory timing differences.

293 In the visual system, asymmetrical length and branching of the dendrites drives temporal
294 disparities in the pattern of inhibition of ganglion cells, providing directional tuning to
295 object movement (Bloomfield, 1994, 1991; Trenholm et al., 2011). The computation in the
296 auditory system differs from vision in several fundamental ways. In the retina, spatial
297 information is directly represented at the level of the photoreceptors, and tuning to spatial
298 movement relies on the relative arrival times of excitatory and inhibitory inputs to the
299 dendrites and soma. By contrast, in the cochlea space is not explicitly represented on the
300 basilar membrane, which decomposes complex sounds spatially into different frequency
301 channels. Accordingly, horizontal spatial receptive fields must be constructed *de novo* in
302 the MSO through the detection of synaptic binaural coincidence. In this way, ITDs serve
303 as a proxy for horizontal position.

304 *Other sources of asymmetry in binaural coincidence detection*

305 Although our data reveal that the dendrites may contribute significant interaural delays in
306 the binaural circuitry in the MSO, they likely work together with other mechanisms that
307 have been proposed to influence binaural coincidence detection. In ~25% of MSO
308 neurons in gerbils, the axon emerges from either the lateral or medial
309 dendrites (Rautenberg et al., 2009; Scott et al., 2005) , and these results appear to extend
310 to other mammalian species, including guinea pigs and cats (Cajal., 1907; Smith, 1995) .
311 Results from computer models suggest these offset axons, like asymmetrical dendrites,
312 introduce strong asymmetries in synaptic integration and ITD tuning (Zhou et al., 2005) .

313 Inhibition has received considerable attention as a mechanism for ITD tuning based on
314 shifts of tuning curves measured in single-unit recordings *in vivo* upon iontophoretic block

315 of glycinergic synapses (Brand et al., 2002; Pecka et al., 2008) . However, these results
316 are controversial, as strong inhibition has not been observed in both juxtacellular and
317 intracellular patch recordings *in vivo* (Franken et al., 2015; Plauska et al., 2016; Roberts
318 et al., 2013), and there have been concerns about iontophoretic strychnine having off-
319 target effects that that alter both firing probability and input resistance (Franken et al.,
320 2015). We found that inhibition did not shift the overall location of ITD curves across the
321 functional range of IPSP magnitudes *(*Fig. 7), consistent with pressure-applied strychnine
322 data *in vivo* (Franken et al., 2015). Inhibition shifted the location of maximal change in
323 firing rate, consistent with a conventional "iceberg" model of inhibitory action on neuronal
324 receptive fields. In mammals, the maximum rate of change, or slope of ITDs may be more
325 important for population encoding of ITDs. Given that the maximal rising slope of firing
326 invariably shifts toward 0 μs ITD when inhibition narrows ITD curves, both inhibition and
327 dendritic asymmetry would both play key roles in setting the location of individual MSO
328 neurons' receptive fields.

329 *Comparison with avian binaural coincidence detectors.*

330 Binaural coincidence detection has been extensively studied in birds, and thus the
331 comparison to mammals is noteworthy. Unlike mammals, dendritic morphology in bird
332 MSO (nucleus laminaris) shows striking dependence on tonotopic location, exhibiting
333 longer, more highly branched dendrites in neurons from low frequency regions (Smith and
334 Rubel, 1979; Wang and Rubel, 2008). While these tonotopic differences in dendritic
335 length have garnered considerable attention, a close examination of dendritic parameters
336 shows that nucleus laminaris neurons, like those in mammalian MSO, exhibit a continuum
337 of dendritic asymmetry in the length of dendrites receiving ipsilateral and contralateral

338 inputs (Smith and Rubel 1979, their Fig. 15 [33]). In these low frequency regions, inputs are
339 restricted to distal, higher order branches (Yamada and Kuba, 2021). Based on both our
340 electrophysiological and modeling data, these higher order branches incur the largest
341 delays as compared to the large-caliber primary dendrites and thus would be the primary
342 determinants of dendritic propagation delay on each side. In the more highly specialized
343 barn owls, the dendrites of laminaris neurons are more limited, and thus internal delay
344 compensation must lie squarely on those provided by unmyelinated afferents (Carr and
345 Konishi, 1990) .

346 *Dendritic morphology and the scaling problem across species.*

347 The biological range of ITDs varies with head size (Jones et al., 2011; Koka et al., 2011) ,
348 and thus any mechanism of internal delay must be scalable across species, accounting
349 for ITDs differing by hundreds of microseconds (e.g., gerbil: ±130 μs (Maier and Klump,
350 2006) , human: ± 600-700 μs (George, 1977)). A dendrite-based source of internal delay
351 would be easily scalable, as the length of MSO dendrites increases with the size of
352 different species. Although quantitative data are not available, previous morphological
353 studies in guinea pig, ferret, cat and humans show that the dendritic arbors show
354 considerable asymmetries (Cajal., 1907; Henkel and Brunso-Bechtold, 1990; Kulesza,
355 2008; Smith, 1995) .

356

357 **METHODS**

358 All procedures were conducted in agreement with the Institutional Animal Care and Use
359 Committee at The University of Texas at Austin (UT-Austin), which followed the guidelines

360 of the National Institutes of Health. Mongolian gerbils (*Meriones unguiculatus*) were
361 housed and raised in a colony at the UT-Austin Animal Resource Center. Animals
362 experienced a 50/50 day/night cycle and had continuous access to food and water.

363 *Brain slice preparation*: both male and female gerbils (17-40 days old) were anesthetized
364 with isoflurane and decapitated upon loss of the choroid reflex. The brain was removed
365 from the cranium under warm (34-35°C) artificial cerebrospinal fluid (ACSF), the
366 cerebellum was removed and the isolated hindbrain was glued to the stage of an
367 oscillating tissue slicer (Leica VT-1200S). Horizontal sections were prepared at 200 μm
368 thickness and stored at 35°C in a holding chamber for 45-60 min., and then gradually
369 cooled to room temperature (24°C). All solutions were continuously bubbled with
370 95% O_2 / 5% CO_2. ACSF contained (in mM): 125 mM NaCl, 25 mM D-glucose, 2.5 mM
371 KCl, 25 mM $NaHCO_3$, 1.25 mM NaH_2PO_4, 1.5mM $MgSO_4$, 1.5 mM $CaCl_2$, pH adjusted to
372 7.45 with NaOH, and final osmolarity at 315 mOsm.

373 *Imaging and electrophysiological acquisition and analyses:* neurons in the MSO were
374 visualized under gradient contrast optics on a Leica TCS SP5 System equipped with a
375 Coherent Chameleon Ultra II Ti:sapphire laser and an 8 kHz resonant scanner under
376 control of Leica LAS AF Imaging Software. We found that gradient contrast images
377 acquired via the photomultiplier tubes were of poor contrast in the heavily myelinated
378 regions of the auditory brainstem, and so cell selection and seal formation was carried
379 out under gradient contrast imaging through the epifluorescence port of the microscope
380 and detected on a high-resolution monochrome digital camera (Zeiss Axiocam 503)
381 running Zen software. The soma was recorded in whole-cell current clamp mode with a
382 pipette (4 to 8 MΩ resistance) containing a potassium gluconate-based solution with 40-

383 80 μM Alexa 594 added for visualizing cell morphology. After waiting ~10 min. for the dye
384 to fill the dendritic arbor, a dendritic recording was made under 2-photon fluorescence
385 with a second pipette (8 to 15 MΩ resistance) containing the same K Gluconate solution
386 with 40-80 μM Alexa 488. Pipette solutions had a composition of 115 mM K-gluconate,
387 4.42 mM KCl, 0.5 mM EGTA, 10 mM HEPES, 10 mM, Na_2Phosphocreatine, 4 mM MgATP,
388 and 0.3 mM NaGTP. Osmolality was adjusted to 300 mOsm/L with sucrose, and pH was
389 adjusted to 7.30 with KOH. Seal resistances exceeded 1 GΩ, and recordings were
390 discontinued if series resistances exceeded 20 or 50 MΩ for somatic and dendritic
391 recordings, respectively.
392 Electrophysiological recordings were under the control of custom routines written in
393 IGOR-Pro (Wavemetrics). Pipettes were prepared on a Sutter P-1000 puller using
394 borosilicate glass (1.5 mm O.D.). Data was acquired using a pair of Dagan BVC-700,
395 amplifiers in conjunction with an ITC-18 computer interface (Heka Instruments). Data was
396 low-pass filtered at 5 kHz, sampled at 50 kHz, and stored on a Macintosh computer for
397 further analyses using custom-written routines in IGOR-Pro.

398 *Compartment model construction:*

399 A subpopulation of 40 fully intact reconstructed MSO neurons was selected from those
400 gathered in Bondy et al. (2021) (Bondy et al., 2021) . The reconstructed morphologies
401 were imported into the NEURON simulation environment, using its Neurolucida importing
402 tool. Computational compartments were created every 2 μm (Fig. S5a). Somatic and
403 dendritic compartments were applied channel kinetics differentially, consisting of low and
404 high-voltage-activated K channels (Mathews et al., 2010; Nabel et al., 2019) , HCN
405 channels(Khurana et al., 2012) , and leak channels, with sodium channels(Scott et al.,

2010) exclusively in the somatic compartments. In simulations modeling a passive cell, high and low-voltage potassium and HCN channels were replaced with passive leak channels with conductances set to the average resting conductance of the preexisting active channels. In simulations with an axon, a model axon, with morphology as in Lehnert (2014) (Lehnert et al., 2014) , was attached at the center of the model soma. The axon channel kinetics implemented consisted of sodium channels, low-threshold potassium channels and leak channels in the nodes and initial segments, with solely leak channels in the internodes. Measurements from the axon were all recorded from the fifth node. Simulated synapses were conductance-based and shaped by an alpha function (τ = 290 μs).

Channel	Dendrite	Soma	TAIS	CAIS	Internode	Node
KLT (Mathews, 2010)	20	40	155	155		155
KHT (Nabel, 2019)	0.55	0.55				
HCN (Khurana, 2011)	1	1	2	2		
Na (Scott, 2010)	0	30	250	250		250
Leak	0.05	0.05	0.05	0.05	0.02	5

Table 1: Maximal channel conductances (μS/cm^2). Tapered axon initial segment (TAIS) and constant disameter axon initial segment (CAIS).

Simulation variations: When measuring EPSP propagation, synapses were placed every 2 μm, with a unitary conductance that would maximally depolarize the soma 1 mV (unless noted otherwise). Each synapse was then stimulated and recorded separately. In ITD

420 coincident detection procedures, dendrites were innervated with synapses (release
421 probability=0.45) placed every 2 μm, totaling ~125 synapses for each side (Couchman et
422 al., 2010) . To mimic axonal activation, an artificial axonal input delay (Δt_{axon}) was
423 calculated for each synapse as a function of conduction velocity (ν_{input}) and axonal travel
424 distance. The travel distance was considered zero at each side's furthest point from the
425 soma. Otherwise, the axonal travel distance consists of two components: the mediolateral
426 distance from the furthest point (Δt_{axon}=0) to the synapse's closest terminal segment; the
427 path length from that terminal segment to the synapse (Fig. S5b). Artificial ITDs could
428 then be added onto the calculated axonal delay. Each artificial ITD value (-0.5 to 0.5 ms,
429 incremented by 0.01), was tested with 400 trials, and each trial consisted of a single
430 stimulation of all synapses. To provide a more binary output, a model axon was attached
431 to the cell's soma, and a spike was reported if a 25 mV depolarization from rest was
432 recorded at the fifth and final axonal node. The synapses could then be adjusted with a
433 unitary conductance to achieve an acceptable maximum firing probability. When
434 implementing IPSP inputs to the ITD procedure, two inhibitory synapses were added at
435 the soma, one corresponding to each mediolateral side. Each synapse generated an
436 IPSP shaped by an alpha function with a time constant of 1.5 ms (Couchman et al.,
437 2010) . The timing of the synapses was adjusted relative to the artificial excitatory ITD
438 signals. The amplitude of the IPSPs was adjusted by modifying the inhibitory synapses'
439 conductances to achieve a combined IPSP hyperpolarization of approximately 1, 2, and
440 3 mV.

441 *Data analyses*

Measures of dendritic distance, both in slice experiments and in compartment models, were taken as the length along the dendritic arbor to the center of the somatic compartment. To address the variable size of the MSO within the slice plane, a normalized tonotopic location was calculated as the cell's distance from the most dorsal point of the MSO, relative to the entire MSO dorsoventral length. To provide a quantitative value of asymmetry between each cell's morphological measures, a unit of fold difference $\left(\log_2\left(\frac{\max\{\text{medial, lateral}\}}{\min\{\text{medial, lateral}\}}\right)+1\right)$ was used, with a value of 1 and 2 representing equal and double values, respectively. Average path length measurements were taken from the distances along the dendrite to the soma from each terminal section of the corresponding mediolateral arbor. Measurements for propagation attenuation and timing were taken at both the synaptic and somatic compartments of the model cell. For attenuation, the somatic depolarization for mediolateral sides was calculated by averaging each synaptic compartments propagated EPSP amplitude at the soma. Morpho-electrotonic transforms were created by scaling each sections length according to the natural logarithm of its attenuation $\left(\text{section length} = \ln\left(\frac{V_{dend}}{V_{soma}}\right)\right)$. EPSP delay values were calculated by measuring the time between peak depolarization in the synaptic and somatic compartments. The corresponding delay transforms are scaled according to the delay contribution of each section. Mediolateral comparisons of delay were calculated by subtracting each sides average EPSP delay for all compartments. To minimize noise and data filtering for the ITD response, the centroid of the curve was measured, where half of the total area under the curve exists on either side. Comparisons were made using the absolute ITD centroid values to highlight the population of neurons' collective change.

The ITD firing probabilities were smoothed with a Savitzky–Golay filter for the purpose of reasonably identifying the region of max slope for the curves.

REFERENCES

Agmon-Snir H, Carr CE, Rinzel J. 1998. The role of dendrites in auditory coincidence detection. Nature **393**:268–272. DOI: https://doi.org/10.1038/30505, PMID: 9607764

Beckius GE, Batra R, Oliver DL. 1999. Axons from anteroventral cochlear nucleus that terminate in medial superior olive of cat: observations related to delay lines. J Neurosci **19**:3146–3161. PMID: 10191328

Bloomfield SA. 1994. Orientation-sensitive amacrine and ganglion cells in the rabbit retina. Journal of Neurophysiology **71**:1672–1691. DOI: https://doi.org/10.1152/jn.1994.71.5.1672, PMID: 8064341

Bloomfield SA. 1991. Two types of orientation-sensitive responses of amacrine cells in the mammalian retina. Nature **350**:347–350. DOI: https://doi.org/10.1038/350347a0, PMID: 1706822

Bondy BJ, Haimes DB, Golding NL. 2021. Physiological diversity influences detection of stimulus envelope and fine structure in neurons of the medial superior olive. J Neurosci. DOI: https://doi.org/10.1523/jneurosci.2354-20.2021, PMID: 34083255

Branco T, Clark BA, Häusser M. 2010. Dendritic discrimination of temporal input sequences in cortical neurons. Science (New York, N.Y.) **329**:1671–1675. DOI: https://doi.org/10.1126/science.1189664

Brand A, Behrend O, Marquardt T, McAlpine D, Grothe B. 2002. Precise inhibition is essential for microsecond interaural time difference coding. Nature **417**:543–547. DOI: https://doi.org/10.1038/417543a, PMID: 12037566

Cajal. SRY. 1907. Structure et connexions des neurones. Nordiskt Medicinskt Arkiv **40**:1–28. DOI: https://doi.org/10.1111/j.0954-6820.1907.tb00034.x

Callan AR, Hess M, Felmy F, Leibold C. 2021. Arrangement of Excitatory Synaptic Inputs on Dendrites of the Medial Superior Olive. J Neurosci **41**:269–283. DOI: https://doi.org/10.1523/jneurosci.1055-20.2020, PMID: 33208467

Carr C, Konishi M. 1990. A circuit for detection of interaural time differences in the brain stem of the barn owl. The Journal of Neuroscience.

Carr CE, Konishi M. 1988. Axonal delay lines for time measurement in the owl's brainstem. Proceedings of the National Academy of Sciences of the United States of America **85**:8311–8315.

Carr CE, Soares D, Parameshwaran S, Perney T. 2001. Evolution and development of time coding systems. Current Opinion in Neurobiology **11**:727–733. DOI: https://doi.org/10.1016/s0959-4388(01)00276-8

503 Couchman K, Grothe B, Felmy F. 2010. Medial superior olivary neurons receive surprisingly few
504 excitatory and inhibitory inputs with balanced strength and short-term dynamics. J Neurosci
505 **30**:17111–17121. DOI: https://doi.org/10.1523/jneurosci.1760-10.2010, PMID: 21159981

506 Dasika VK, White JA, Colburn HS. 2007. Simple models show the general advantages of
507 dendrites in coincidence detection. J Neurophysiol **97**:3449–3459. DOI:
508 https://doi.org/10.1152/jn.00669.2005, PMID: 16914612

509 Feng AS, Rogowski BA. 1980. Effects of monaural and binaural occlusion on the morphology of
510 neurons in the medial superior olivary nucleus of the rat. Brain Research **189**:530–534. DOI:
511 https://doi.org/10.1016/0006-8993(80)90112-2, PMID: 7370789

512 Franken TP, Bremen P, Joris PX. 2014. Coincidence detection in the medial superior olive:
513 Mechanistic implications of an analysis of input spiking patterns. Frontiers in Neural Circuits
514 **8**:42. DOI: https://doi.org/10.3389/fncir.2014.00042, PMID: 24822037

515 Franken TP, Roberts MT, Wei L, Golding NL, Joris PX. 2015. In vivo coincidence detection in
516 mammalian sound localization generates phase delays. Nat Neurosci **18**:444–452. DOI:
517 https://doi.org/10.1038/nn.3948, PMID: 25664914

518 George K. 1977. Model for the intramural time differences in the azimuthal plane. J. Acoust.
519 Soc. Am **62**:157–167.

520 Goldberg JM, Brown PB. 1969. Response of binaural neurons of dog superior olivary complex
521 to dichotic tonal stimuli: some physiological mechanisms of sound localization. J
522 Neurophysiol **32**:613–636.

523 Grothe B, Pecka M. 2014. The natural history of sound localization in mammals--a story of
524 neuronal inhibition. Front Neural Circuits **8**:116. DOI:
525 https://doi.org/10.3389/fncir.2014.00116, PMID: 25324726

526 Heijden M van der, Lorteije JA, Plauska A, Roberts MT, Golding NL, Borst JG. 2013. Directional
527 hearing by linear summation of binaural inputs at the medial superior olive. Neuron **78**:936–
528 948. DOI: https://doi.org/10.1016/j.neuron.2013.04.028, PMID: 23764292

529 Henkel CK, Brunso-Bechtold JK. 1990. Dendritic morphology and development in the ferret
530 medial superior olivary nucleus. J Comp Neurol **294**:377–388. DOI:
531 https://doi.org/10.1002/cne.902940307, PMID: 2341617

532 Hoffmeister B, Jänig W, Lisney SJW. 1991. A proposed relationship between circumference and
533 conduction velocity of unmyelinated axons from normal and regenerated cat hindlimb
534 cutaneous nerves. Neuroscience **42**:603–611. DOI: https://doi.org/10.1016/0306-
535 4522(91)90402-a

536 Jeffress LA. 1948. A place theory of sound localization. J Comp Physiol Psychol **41**:35–39.
537 PMID: 18904764

538 Jercog P. 2008. Study of different physiological components that underlie interaural time delay
539 detection in the auditory system. NYU Department of Physics Dissertation.

Jercog PE, Svirskis G, Kotak VC, Sanes DH, Rinzel J. 2010. Asymmetric excitatory synaptic dynamics underlie interaural time difference processing in the auditory system. PLoS Biol **8**:e1000406. DOI: https://doi.org/10.1371/journal.pbio.1000406, PMID: 20613857

Jones HG, Koka K, Thornton JL, Tollin DJ. 2011. Concurrent development of the head and pinnae and the acoustical cues to sound location in a precocious species, the chinchilla (Chinchilla lanigera). J Assoc Res Otolaryngol **12**:127–140. DOI: https://doi.org/10.1007/s10162-010-0242-3, PMID: 20957506

Joris P, Yin TC. 2007. A matter of time: internal delays in binaural processing. Trends Neurosci **30**:70–78. DOI: https://doi.org/10.1016/j.tins.2006.12.004, PMID: 17188761

Kapfer C, Seidl AH, Schweizer H, Grothe B. 2002. Experience-dependent refinement of inhibitory inputs to auditory coincidence-detector neurons. Nat Neurosci **5**:247–253. DOI: https://doi.org/10.1038/nn810, PMID: 11850629

Khurana S, Liu Z, Lewis AS, Rosa K, Chetkovich D, Golding NL. 2012. An essential role for modulation of hyperpolarization-activated current in the development of binaural temporal precision. J Neurosci **32**:2814–2823. DOI: https://doi.org/10.1523/jneurosci.3882-11.2012, PMID: 22357864

Koka K, Jones HG, Thornton JL, Lupo JE, Tollin DJ. 2011. Sound pressure transformations by the head and pinnae of the adult Chinchilla (Chinchilla lanigera). Hear Res **272**:135–147. DOI: https://doi.org/10.1016/j.heares.2010.10.007, PMID: 20971180

Kulesza R. 2008. Cytoarchitecture of the human superior olivary complex: nuclei of the trapezoid body and posterior tier. Hear Res **241**:52–63. DOI: https://doi.org/10.1016/j.heares.2008.04.010, PMID: 18547760

Lehnert S, Ford MC, Alexandrova O, Hellmundt F, Felmy F, Grothe B, Leibold C. 2014. Action potential generation in an anatomically constrained model of medial superior olive axons. J Neurosci **34**:5370–5384. DOI: https://doi.org/10.1523/jneurosci.4038-13.2014, PMID: 24719114

Lindsey BG. 1975. Fine structure and distribution of axon terminals from the cochlear nucleus on neurons in the medial superior olivary nucleus of the cat. J Comp Neurol **160**:81–103. DOI: https://doi.org/10.1002/cne.901600106, PMID: 1112923

Magnusson AK, Kapfer C, Grothe B, Koch U. 2005. Maturation of glycinergic inhibition in the gerbil medial superior olive after hearing onset. J Physiol **568**:497–512. DOI: https://doi.org/10.1113/jphysiol.2005.094763, PMID: 16096336

Maier JK, Klump GM. 2006. Resolution in azimuth sound localization in the Mongolian gerbil (Meriones unguiculatus) . The Journal of the Acoustical Society of America **119**:1029–1036. DOI: https://doi.org/10.1121/1.2159429, PMID: 16521765

Mathews PJ, Jercog PE, Rinzel J, Scott LL, Golding NL. 2010. Control of submillisecond synaptic timing in binaural coincidence detectors by K(v)1 channels. Nat Neurosci **13**:601–609. DOI: https://doi.org/10.1038/nn.2530, PMID: 20364143

578 Moiseff A, Konishi M. 1981. Neuronal and behavioral sensitivity to binaural time differences in
579 the owl. The Journal of Neuroscience: The Official Journal of the Society for Neuroscience
580 **1**:40–48. DOI: https://doi.org/10.1523/jneurosci.01-01-00040.1981

581 Myoga MH, Lehnert S, Leibold C, Felmy F, Grothe B. 2014. Glycinergic inhibition tunes
582 coincidence detection in the auditory brainstem. Nat Commun **5**:3790. DOI:
583 https://doi.org/10.1038/ncomms4790, PMID: 24804642

584 Nabel AL, Callan AR, Gleiss SA, Kladisios N, Leibold C, Felmy F. 2019. Distinct distribution
585 patterns of potassium channel sub-units in somato-dendritic compartments of neurons of the
586 medial superior olive. Frontiers in Cellular Neuroscience **13**:409471. DOI:
587 https://doi.org/10.3389/fncel.2019.00038/bibtex

588 Pecka M, Brand A, Behrend O, Grothe B. 2008. Interaural time difference processing in the
589 mammalian medial superior olive: the role of glycinergic inhibition. J Neurosci **28**:6914–6925.
590 DOI: https://doi.org/10.1523/jneurosci.1660-08.2008, PMID: 18596166

591 Plauska A, Borst JG, Heijden M van der. 2016. Predicting binaural responses from monaural
592 responses in the gerbil medial superior olive. J Neurophysiol **115**:jn 01146 2015. DOI:
593 https://doi.org/10.1152/jn.01146.2015, PMID: 27009164

594 Plauška A, Heijden MVD, Borst JGG. 2017. A test of the stereausis hypothesis for sound
595 localization in mammals. Journal of Neuroscience **37**:7278–7289. DOI:
596 https://doi.org/10.1523/jneurosci.0233-17.2017, PMID: 28659280

597 Rautenberg PL, Grothe B, Felmy F. 2009. Quantification of the three-dimensional morphology of
598 coincidence detector neurons in the medial superior olive of gerbils during late postnatal
599 development. J Comp Neurol **517**:385–396. DOI: https://doi.org/10.1002/cne.22166, PMID:
600 19760600

601 Rinzel J, Rall W. 1974. Transient response in a dendritic neuron model for current injected at
602 one branch. Biophysical Journal **14**:759–790. DOI: https://doi.org/10.1016/s0006-
603 3495(74)85948-5

604 Roberts MT, Seeman SC, Golding NL. 2013. A mechanistic understanding of the role of
605 feedforward inhibition in the mammalian sound localization circuitry. Neuron **78**:923–935.
606 DOI: https://doi.org/10.1016/j.neuron.2013.04.022, PMID: 23764291

607 Russell FA, Moore DR. 1999. Effects of unilateral cochlear removal on dendrites in the gerbil
608 medial superior olivary nucleus. Eur J Neurosci **11**:1379–1390.

609 Scott LL, Mathews PJ, Golding NL. 2010. Perisomatic voltage-gated sodium channels actively
610 maintain linear synaptic integration in principal neurons of the medial superior olive. J
611 Neurosci **30**:2039–2050. DOI: https://doi.org/10.1523/jneurosci.2385-09.2010, PMID:
612 20147532

613 Scott LL, Mathews PJ, Golding NL. 2005. Posthearing developmental refinement of temporal
614 processing in principal neurons of the medial superior olive. J Neurosci **25**:7887–7895. DOI:
615 https://doi.org/10.1523/jneurosci.1016-05.2005, PMID: 16135745

616 Shamma SA, Shen N, Gopalaswamy P. 1989. Stereausis: binaural processing without neural
617 delays. The Journal of the Acoustical Society of America **86**:989–1006. DOI:
618 https://doi.org/10.1121/1.398734, PMID: 2794252

619 Smith DJ, Rubel EW. 1979. Organization and development of brain stem auditory nuclei of the
620 chicken: dendritic gradients in nucleus laminaris. J Comp Neurol **186**:213–239. DOI:
621 https://doi.org/10.1002/cne.901860207, PMID: 447882

622 Smith PH. 1995. Structural and functional differences distinguish principal from nonprincipal
623 cells in the guinea pig MSO slice. Journal of Neurophysiology **73**:1653–1667. DOI:
624 https://doi.org/10.1152/jn.1995.73.4.1653, PMID: 7643173

625 Smith PH, Joris PX, Carney LH, Yin TC. 1991. Projections of physiologically characterized
626 globular bushy cell axons from the cochlear nucleus of the cat. J Comp Neurol **304**:387–407.
627 DOI: https://doi.org/10.1002/cne.903040305, PMID: 2022755

628 Smith PH, Joris PX, Yin TC. 1993. Projections of physiologically characterized spherical bushy
629 cell axons from the cochlear nucleus of the cat: evidence for delay lines to the medial
630 superior olive. J Comp Neurol **331**:245–260. DOI: https://doi.org/10.1002/cne.903310208,
631 PMID: 8509501

632 Spitzer MW, Semple MN. 1995. Neurons sensitive to interaural phase disparity in gerbil superior
633 olive: diverse monaural and temporal response properties. J Neurophysiol **73**:1668–1690.

634 Stotler WA. 1953. An experimental study of the cells and connections of the superior olivary
635 complex of the cat. J Comp Neurol **98**:401–431.

636 Trenholm S, Johnson K, Li X, Smith RG, Awatramani GB. 2011. Parallel mechanisms encode
637 direction in the retina. Neuron **71**:683–694. DOI:
638 https://doi.org/10.1016/j.neuron.2011.06.020, PMID: 21867884

639 Wang Y, Rubel EW. 2008. Rapid regulation of microtubule-associated protein 2 in dendrites of
640 nucleus laminaris of the chick following deprivation of afferent activity. Neuroscience
641 **154**:381–389. DOI: https://doi.org/10.1016/j.neuroscience.2008.02.032

642 Werthat F, Alexandrova O, Grothe B, Koch U. 2008. Experience-dependent refinement of the
643 inhibitory axons projecting to the medial superior olive. Dev Neurobiol **68**:1454–1462. DOI:
644 https://doi.org/10.1002/dneu.20660, PMID: 18777566

645 Winters BD, Jin SX, Ledford KR, Golding NL. 2017. Amplitude Normalization of Dendritic
646 EPSPs at the Soma of Binaural Coincidence Detector Neurons of the Medial Superior Olive.
647 J Neurosci **37**:3138–3149. DOI: https://doi.org/10.1523/jneurosci.3110-16.2017, PMID:
648 28213442

649 Yamada R, Kuba H. 2021. Dendritic synapse geometry optimizes binaural computation in a
650 sound localization circuit. Science Advances **7**. DOI: https://doi.org/10.1126/sciadv.abh0024,
651 PMID: 34818046

652 Yin TC, Chan JC. 1990. Interaural time sensitivity in medial superior olive of cat. J Neurophysiol
653 **64**:465–488. PMID: 2213127

654 Zhou Y, Carney LH, Colburn HS. 2005. A model for interaural time difference sensitivity in the
655 medial superior olive: interaction of excitatory and inhibitory synaptic inputs, channel
656 dynamics, and cellular morphology. J Neurosci **25**:3046–3058. DOI:
657 https://doi.org/10.1523/jneurosci.3064-04.2005, PMID: 15788761

658